

GALILEO NIMS NEAR-INFRARED OBSERVATIONS OF JUPITER'S RING SYSTEM

Stuart McMuldroy¹, G. Edward Danielson^{1,2}, Stuart H. Pilorz²

and the NIMS Science Team

1. Division of Geological and Planetary Sciences

California Institute of Technology, Pasadena, CA 91125

2. Jet Propulsion Laboratory

California Institute of Technology, Pasadena, CA 91109

Submitted to *ICARUS*

Address all correspondence to first author at sxm@hellas.gps.caltech.edu

Total number of pages: 25

Number of Tables:

Number of Figures: 10

Keywords: Jupiter; planetary rings; planetary rings, Jupiter; infrared observations

October 14, 1998

Running Head: Galileo NIMS Near-Infrared Observations of Jupiter's Ring
System

Please direct all proofs to:

Stuart McMuldroy
Division of Geological and Planetary Sciences
California Institute of Technology, MS 150-21
Pasadena, CA 91125
FAX 626 585-1917

ABSTRACT

*planetary rings
infrared observations*

We present the first observations of the Jovian ring system viewed at near-infrared wavelengths in forward-scattered light. The eclipse of the Sun by Jupiter during the “C3” orbit of the Galileo spacecraft afforded favorable conditions for the Near Infrared Mapping Spectrometer (NIMS) to observe the ring system between $0.7 - 5.2 \mu\text{m}$ at a spectral resolution of $\approx 0.04 \mu\text{m}$. NIMS images show the nearly edge-on main ring from just inside the ansa at $1.80 R_J$ down to $1.05 R_J$, at a spatial resolution of 1130 km . Profiles across the ring plane reveal the faint halo interior to the main ring and extending $>6500 \text{ km}$ either side of the ring plane. At these spatial resolutions, no fine structure is apparent in either the ring or halo. The large wavelength coverage of the NIMS observations permits an analysis of the scattering properties of the ring system even though the ring subtends only a small range of scattering angles. Our retrieved particle size distribution exhibits a roughly linear trend with a relative abundance of particles of radii between $1 \mu\text{m}$ and $18 \mu\text{m}$. The linear trend is best described as a power law with index $p = 3.9 \pm 0.2$ while the relative surfert is best modeled by a combined normal and gamma distribution. Analysis shows that Voyager data lacked the required wavelength coverage and viewing geometry to determine the particle distribution uniquely. We conclude that the NIMS data set is a better determinant of the particle size distribution, especially for particles larger than a micron. We speculate that the power law distribution is attributable to halo particles while the surfert between $1 \mu\text{m}$ and $18 \mu\text{m}$ is due to particles in the main ring. If so, this difference in size distributions implies that particles in the main ring are being modified prior to ejection into the halo.

1. Introduction

The Jovian ring was first discovered in images from the Voyager spacecraft (Owen *et al.* 1979, Smith *et al.* 1979, Jewitt and Danielson 1981, Burns *et al.* 1984, Showalter *et al.* 1985, 1987), although its presence had been previously inferred from particle flux measurements (Smoluchowski 1976). Ground based observations have been conducted at visible wavelengths (Smith and Reitsema 1980), near-infrared wavelengths (Jewitt *et al.* 1981; Nicholson and Matthews 1991), and in the infrared (Becklin and Wynn-Williams 1979; Neugebauer *et al.* 1981). Extensive analyses of the Voyager images (Jewitt and Danielson 1981; Showalter *et al.* 1987) reveal a main ring 7000 km wide with an outer boundary at $129,200 \pm 700$ km ($1.81 \pm 0.01 R_J$) and of low optical depth ($\tau \approx 1-6 \times 10^{-6}$). Exterior to this, out to 210,000 km, is a far fainter “gossamer” ring (Showalter *et al.* 1985). Interior to the main ring is a vertically extended halo that has been postulated as being either lenticular (Jewitt and Danielson 1981), or toroidal (Showalter *et al.* 1987). Analysis of the visible wavelength data from the Voyager spacecraft suggests the ring particles obey a power law size distribution with the smaller grains originating as impact eject from the collisions between larger bodies (Showalter *et al.* 1987). Dynamical arguments suggest the ring material is replenished every $\approx 10^3$ years (Burns *et al.* 1984). Ring particles may originate from the Jovian satellites Metis and Adrastea, as suggested by the red color of the ring and satellites. Electromagnetic effects are thought to control the resulting ring structure (Consolmagno 1980; Morfill *et al.* 1980; Burns *et al.* 1985; Horányi and Cravens 1996).

2. Observations

We present results from analysis of data obtained with the Near Infrared Mapping Spectrometer (NIMS) instrument aboard the Galileo spacecraft which is currently orbiting Jupiter. The NIMS instrument is a multi-spectral ($0.7 - 5.2 \mu\text{m}$) variable resolution spectrometer that has been described in detail previously (Carlson *et al.* 1992). The NIMS instrument acquired multi-spectral images of the eastern ansa of the Jovian ring system during November 11, 1996 while in the “C3” orbit (for Galileo observation plans see Wolf and Byrnes 1993, and Smythe *et al.* 1995). NIMS acquired ring data in five separate segments, located contiguously along the ring. For this period, Jupiter eclipsed the Sun enabling the faint ring to be seen in strongly forward-scattered light. At an average distance of $\approx 2.26 \times 10^6$ km from the ring, and lying 0.5° above the ring plane, the instrument’s scan rate along the ring plane yielded a spatial resolution of ≈ 1130 km/pixel sampled at the Nyquist frequency of 450 km/pixel. The ring was seen nearly edge-on and at phase angles of around $\approx 178.8^\circ$. For these observations, the instrument’s average spectral resolution was $\approx 0.04 \mu\text{m}$ with 102 bands covering the $0.7 - 5.2 \mu\text{m}$ wavelength range. These are the first observations of the Jovian ring system made at near-infrared wavelengths in forward-scattered light. At these spatial and spectral resolutions, the NIMS data reveal the macro structure of the rings at moderate spectral resolution. These data extend and complement the high resolution but spectrally limited data from the Voyager and Galileo’s SSI cameras.

3. Results

3.1 Standard Calibration and Image Reconstruction

Standard NIMS calibration techniques were first applied to the data. These include applying offset biases and multiplicative factors to the raw data to allow the removal of the instrument signature. More details pertaining to NIMS calibration techniques can be found in Carlson 1981 and Carlson *et al.* 1992.

Following calibration, the individual data segments were combined to produce one continuous image of the ring. The resulting data cube measures 20 lines across the projected ring plane, 120 samples along the ring plane, with 102 wavelength bands. Each pixel measures approximately 450 km along the ring plane by 1130 km out of the ring plane. This data cube therefore covers a region approximately 22600 x 54000 km between the wavelengths 0.7 – 5.2 μm . Data taken between 2.36 – 2.67 μm was removed as it was corrupted due to a faulty detector.

3.2 Processed Images and Preliminary Analysis

Figure 1a shows the calibrated NIMS image of the Jovian ring system at 1.31 μm in forward-scattered light. This image, like all others presented here, is in dimensionless units of I/F where I is the radiance and πF is the solar flux density at Jupiter's distance from the Sun during the observations. These units allow for easy comparison between different wavelengths as the influence of the solar spectrum has been removed. Jupiter is off to the right while the image extends out to approximately 1.80 R_J . The main ring is apparent in the center of the image, viewed nearly edge-on and highly foreshortened. This viewing geometry coupled with the low

spatial resolution prevents any fine radial structure being seen. Peak intensity in this image is 8.5×10^{-3} , at a distance of $\approx 1.75 R_J$, with a noise level of 0.5×10^{-3} . On larger scales, the ring appears to broaden towards Jupiter due to the increasing projected distance between its near and far arms. At the NIMS spatial resolution, however, the two sides cannot be completely separated. No obvious evidence is seen of the faint halo that has been detected at other wavelengths and viewing angles. This is discussed further in Section 3.3.

Figure 1b shows the main ring at $2.03 \mu\text{m}$. The ring is brightest at this wavelength with a peak of 11.3×10^{-3} , corresponding to a maximum signal to noise of $\approx 9:1$, located at a projected distance of $\approx 1.73 R_J$. The main ring again appears to broaden toward Jupiter and remains the only ring system component that is detected. Several instrument and calibration artifacts are, however, apparent in the image. The most obvious are the regions of missing data, presented in black, in image areas devoid of a strong signal. This is the result of a threshold and compression process being applied to the raw data prior to transmission to Earth in accordance with the constraints of the impaired Galileo telecommunications system. Unfortunately, this process varied by segment and wavelength band resulting in the patch work pattern seen in Fig. 1b. Although this artifact is seen at several different wavelengths, it influences none of the main ring data.

An image of the main ring at a wavelength of $3.51 \mu\text{m}$ is shown in Fig. 1c. The ring, albeit weaker in intensity, retains much of the same structure. The brightest region is located closer to Jupiter with a maximum I/F value of 9.8×10^{-3} at a projected distance of $1.70 R_J$.

3.3 Profiles Measured Along and Across the Ring Plane

Figures 2a-c show vertical profiles taken through the ring plane at locations A, B, C, and D as marked in Fig. 1. These points are located at $1.75 R_J$, $1.55 R_J$, $1.32 R_J$, and $1.09 R_J$, respectively. These four positions were chosen to represent data close to Jupiter (D), close to the ring ansa (A), with two additional points located evenly between. The profiles in Fig. 2a were measured at $1.31 \mu\text{m}$, those in Fig. 2b at $2.03 \mu\text{m}$, and those in Fig. 2c at $3.51 \mu\text{m}$. In each figure, the peak intensity occurs at line 10, the location of the main ring. Lower line values correspond to positions above the ring plane. At all three chosen wavelengths, the profile full-width at half the maximum value increases from A to D approaching Jupiter. This simply corresponds to the increase in the projected distance between the ring arms. The profiles vary in shape, however, depending on location and wavelength. At the shortest wavelength of $1.31 \mu\text{m}$, profiles measured at positions B, C and D show a sharp peak on a platform that extends ± 6 pixels from the main ring. Beyond this the platform signal is insufficient in strength to be distinguished from noise. A similar, albeit much weaker, structure is also seen at $2.03 \mu\text{m}$. The platform is not evident at $3.51 \mu\text{m}$. Position A, closest to the ansa, does not possess a significant platform at any wavelength. These effects are in agreement with scattering by small particles of a micron or smaller in size. These particles would preferentially scatter at the shortest wavelengths observed by NIMS. We infer that this is a detection of the halo that exists interior to the main ring and that extends above and below the ring plane.

Profiles measured along the main ring at wavelengths of 1.31 , 2.03 , and $3.51 \mu\text{m}$ are shown in Fig. 3. The dimensionless I/F values are plotted as a function of projected distance along the ring plane, in units of Jupiter radii. As seen in Fig. 1a, the intensity along the ring plane does not

vary significantly at 1.31 μm . The profile at 2.03 μm exhibits a 20% decrease in intensity from values measured at the ansa to those measured closer to Jupiter. The profile at 3.51 μm shows a similar but greater change, with values decreasing by 50%. These trends are also consistent with the presence of the tenuous ring halo. The sub-micron halo particles would contribute more to the 1.31 μm profile than the 3.51 μm profile. Their contribution would also increase for measurements furthest from the ansa, as the halo is located interior to the main ring. This would result in flatter profiles at shorter wavelengths just as is measured. As the angle subtended is small, this is unlikely to be simply a variation of the phase function across the ring. We therefore conclude this is a detection of halo particles located in the ring plane.

3.4 Ring Spectra

The vertical ring profiles presented in Fig. 2 do not return to $I/F=0$ for regions where there is no signal from either the ring or the halo. Often these offset biases are negative. Normally, such biases are removed during standard calibration. The observations presented here, however, were inordinately difficult as the ring is extremely faint. To remove these remaining biases, and allow a more precise quantitative comparison between wavelengths, an additional calibration step was applied. This was done by subtracting a “sky” cube, constructed from areas of the original image data lacking either ring or halo signal. Pixel areas dominated by noise were selected at positions along the ring but out of the ring plane for every wavelength. These were then interpolated to produce a full sky cube. A simple boxcar-smoothing algorithm was then applied to the cube. The resulting data were checked to confirm that any wavelength dependent structure corresponded to detector boundaries rather than a faint ring signal that had been overlooked in the earlier

analysis. This sky cube was then subtracted from the calibrated image cube to produce a corrected image cube.

Spectra from this corrected data cube are presented in Fig. 4 for positions A through D. Only measurements between 1.0 – 4.0 μm are shown. Outside of this wavelength range the detector noise was sufficiently large to make the ring data unsuitable for quantitative use. The ring is still detectable, albeit very faintly, from 4.0 – 5.2 μm . As mentioned above, the peak ring I/F value occurs at approximately 2.0 μm at A, the position closest the ansa. For the other locations, the peak value occurs at progressively shorter wavelengths approaching Jupiter. Either side of these peaks, the intensity decreases roughly linearly toward both longer and shorter wavelengths. The spectra possess no sharp absorption features. This is expected as the ring is viewed at very high phase angles in forward-scattered light. Diffraction effects dominate for these conditions and the complex component of the index of refraction only weakly influences results. Any spectral signature therefore results from variations in the particle phase function, the particle size distribution, the optical path length through the ring, and any wavelength dependence of the particle single scattering albedo. This is examined further in Section 4.

4. Modeling

4.1 Theory

In this section, we compare the NIMS observations with models of the light scattered by the Jovian ring so as to extract the size distribution of particles in the ring and halo. As the Jovian ring system is so tenuous, we assume in the models that single scattering dominates i.e. light from the sun having hit a ring or halo particle is scattered directly to the NIMS instrument without interacting with any other particles. In these calculations, we also assume that any light reflected from Jupiter's atmosphere does not contribute significantly to the illumination of the rings (see Showalter *et al.* 1987). The observed values of I/F can therefore be related to the ring's

$$\frac{I}{F} = \frac{\omega_0 \tau P(\theta)}{4\mu}$$

optical depth τ , the single scattering albedo ω_0 , and the phase function $P(\theta)$ using

where θ is the scattering angle, $\mu = |\cos \theta|$, and ε is the emission angle (Chandrasekhar 1960).

For the NIMS observations ε is 89.5° and $\mu \approx 1$. The value of $\omega_0 \tau P(\theta)$ can in turn be related to the scattering cross-section σ_{sca} , the phase function $P(\theta)$, and the particle size distribution $n(r)$ using

$$\omega_0 \tau P(\theta) = \int_{r_{\min}}^{r_{\max}} \sigma_{\text{sca}} P(\theta, r) n(r) dr$$

where r is the particle radius, r_{\min} is the minimum particle size, and r_{\max} the maximum particle size used in the calculations. The phase function $P(\theta)$ and scattering cross-section σ_{sca} for a particle can be calculated directly from Mie theory if the particle refractive index is known. At small scattering angles, such as seen in the NIMS observations, diffraction effects produce an intense narrow diffraction lobe. The shape of this lobe is largely insensitive to changes in the refractive index. For these calculations we adopt the value for the refractive index used by Showalter *et al.* (1987) of $1.50 - i0.01$. The NIMS observations are therefore most dependent on the particle size distribution. In Mie theory, the degree of scattering is characterized by the dimensionless parameter $x \dots 2\pi r / \lambda$. Therefore, as the NIMS data cover a large wavelength range, they are good determinants of the ring particle size distribution even though they span a small number of phase angles. For our calculations we assume that although Mie theory is only strictly applicable to scattering by spheres, any deviation from sphericity by the ring particles probably has negligible effect.

4.2 Data Preparation

The Jovian ring system is comprised of a tenuous extended halo interior to a main ring. As the ring system is viewed nearly edge-on in the NIMS data, pixels toward the left of Fig. 1a-c (away from Jupiter) contain light scattered only by ring particles. Pixels closer to Jupiter measure light scattered by particles in both the ring and halo. This geometry is shown in schematic form in Fig. 5a. Region 1 contains just “ring” pixels while region 2 contains “ring and halo” pixels. To avoid

introducing errors by modeling these two different regions together, we split the corrected data cube into two parts corresponding to regions 1 and 2. Unfortunately, region 1 does not span a sufficient range of phase angles to be useful for modeling purposes and was therefore rejected.

Region 2 was sampled to produce a smaller cube so as to reduce the number of modeling calculations. First, lines 9 and 10, that contain light scattered by ring and halo particles lying in the ring plane, were extracted and added together. Second, this summation was sampled at 20 phase angles positioned equidistantly along the ring and at 10 wavelength intervals starting at 1.0 μm .

Figure 5b shows a schematic of the Jovian ring system as viewed from above. The pathlength through the main ring changes as a function of the projected distance from Jupiter for the NIMS observing geometry. Pixels at different positions along the ring therefore measure light integrated over varying column lengths. This effectively introduces a variable optical depth along the ring as $\tau \propto \text{pathlength}$ for the optically thin Jovian ring system. To remove this effect we divided by the pathlength, calculated for a ring of outer and inner radii of $1.81 R_J$ and $1.72 R_J$ respectively, convolved with the instrument spatial resolution (see Carlson *et al.* 1992, Carlson *et al.* 1997). No attempt was made to correct for the geometry of the halo as this is ill defined and the halo intensity is an order of magnitude smaller than that of the ring.

4.3 Modeling the Data

The model calculated scattering phase functions and cross sections for 200 values of the Mie parameter $x \equiv 2\pi r / \lambda$. These values were logarithmically spaced between $x = 0.0124$ and

$x = 392.0$. This corresponds to particle sizes of $0.01 \mu\text{m}$ and $50.0 \mu\text{m}$ for the NIMS wavelengths. We found that expanding these limits had minimal effect on our fits. The individual phase functions were combined and fit to the NIMS data using an iterative method. The relative combinations of the individual functions yielded the particle size distribution. This calculation is most sensitive to particles of roughly similar size to the wavelength of observation. Given the wavelength range of the NIMS observations, realistic particle size distribution estimates can be made for particles of radii from $0.1 \mu\text{m}$ to $50.0 \mu\text{m}$. For these wavelengths, particles smaller than $0.1 \mu\text{m}$ in radius behave as isotropic Rayleigh scatterers and contain no useful phase information. At the other extreme, particles larger than $50.0 \mu\text{m}$ do not behave as Mie scatterers for these wavelengths and our observations are not sensitive to their scattering properties.

Figure 6 shows the NIMS data and the best fit results calculated from the model. The value of $\omega\sigma P(\theta)$ is plotted as a function of scattering angle for the 10 sampled wavelengths. The solid line represents the sampled NIMS observations while the dashed line shows the model results re-normalized by the pathlength. Comparison with visible data at larger scattering angles suggests that diffraction effects intensify the scattered light by a factor of $\approx 10^4$. Analysis reveals that the model is insensitive to changes in the complex component of the refractive index as predicted. The fit is therefore most sensitive to changes in the particle size distribution. Our model, and therefore our calculated particle size distribution, appears to be in excellent agreement with the data. The dotted line represents values that would have been seen if the particle size distribution $n(r)$ had followed a power law of the form

$$n(r)dr = Ar^{-p}dr$$

with a power law index $p = 2.5 \pm 0.5$ and normalization factor $A = 1.71 \text{ cm}^{-2}$. This ring particle distribution was first put forward by Showalter *et al.* (1987) based on analysis of visible data from the Voyager camera. This distribution is offset from the NIMS data. The offset is probably due to differences in the effective optical depth between the data sets as NIMS imaged the ring edge-on while Showalter *et al.* (1987) adopted an optical depth normal to the ring plane. The power law does not, however, follow the trends in scattering angle or wavelength seen in the NIMS data. This discrepancy cannot be easily explained and suggests the power law distribution is inadequate for the particle sizes measured at the scattering angles and wavelengths of the NIMS data.

Figure 7 shows the logarithm of the particle size distribution plotted as a function of the logarithm of the particle radius. Our retrieved particle size distribution is shown as a solid line. The number of particles decreases roughly linearly in logarithmic space as the particle radius increases. Such a linear trend is indicative of a power law distribution in agreement with Showalter *et al.* (1987). There is, however, a sudden increase in the number of particles relative to this trend between $1 \text{ }\mu\text{m}$ and $18 \text{ }\mu\text{m}$. This suggests additional components are needed to fit the data. We find that three components are needed to adequately model the data. We use a power law with $p = 3.95$ and $A = 0.005 \text{ cm}^{-2}$ to reproduce the overall linear trend. The increase between $1 \text{ }\mu\text{m}$ and $18 \text{ }\mu\text{m}$ is best described by the combination of a normal and a gamma distribution. The normal distribution has a mean of 9.1, sigma 1.0, and amplitude 0.3. The gamma distribution has an alpha of 15.0, beta of 0.25, and amplitude of 3.0 where

$$g(r) = \frac{r^{\alpha-1} \exp(-r/\beta)}{\beta^\alpha \Gamma(\alpha)}$$

and $\Gamma(\alpha)$ is the gamma function. This fit is shown in Fig. 7 as a dashed line. For comparison, the power law distribution from Showalter *et al.* (1987) is depicted as a dotted line. Although this power law distribution roughly duplicates the large-scale trends in the particle size distribution it does not predict its fine structure. The Showalter *et al.* (1987) was, however, derived at smaller wavelengths and larger scattering angles. Figure 8 shows $\omega_0 \tau P(\theta)$ plotted as a function of the Voyager scattering angles of 4° to 6° and at 12 wavelengths. The first two wavelength bands on the left of the figure correspond to the wavelengths of the Voyager violet and orange filters. The remaining 10 near-infrared bands correspond to those NIMS wavelengths chosen during our modeling and in Fig. 6. The solid line shows values calculated using our retrieved particle size distribution and the appropriate phase function for scattering angles between 4° and 6° . The dashed line represents data constructed from a power law distribution with $p = 2.5$. Although the values of $\omega_0 \tau P(\theta)$ for the two distributions appear to be nearly the same at optical wavelengths, they diverge towards the infrared. The Voyager data would therefore be inadequate for discriminating between these particle size distributions. We conclude that the NIMS data, due to its wavelength range and preferable viewing geometry, is a better determinant of the ring and halo particle size distribution, especially for particles larger than a micron in radius.

5. Discussion

The eclipse of the Sun by Jupiter during the C3 orbit of the Galileo spacecraft provided favorable conditions for the Near Infrared Mapping Spectrometer (NIMS) to observe the Jovian ring system in strongly forward scattered light. NIMS mapped the nearly edge-on ring system from just inside the main ring ansa around $1.80 R_J$ down to approximately $1.05 R_J$. Spatial resolution in these images is 1130 km with a wavelength resolution of $\approx 0.04 \mu\text{m}$ over the $0.7 - 5.2 \mu\text{m}$ range.

The NIMS observations reveal the main Jovian ring. No radial structure is apparent with this spatial resolution and observing geometry. Profiles taken cross the ring plane show a faint signal extending ≈ 6500 km above and below the ring plane. Beyond this, the signal is too weak to be distinguished from noise. This signal is only present interior to the projected edge of the main ring and at wavelengths shorter than $\approx 2.5 \mu\text{m}$. These observations are consistent with the detection of the extended halo, seen at visible wavelengths, that lies between Jupiter and the main ring and is comprised of sub-micron particles. For these wavelengths, the NIMS observations are the first images of the main Jovian ring and the extended halo in forward-scattered light.

The large wavelength coverage of the NIMS observations permits an analysis of the scattering properties of the main ring even though the ring subtends only a small range of scattering angles. Using a Mie scattering model, we calculated the size distribution of particles in the ring and halo. Our retrieved particle size distribution follows a roughly linear trend with a relative increase in

the number of particles between 1 μm and 18 μm . We find this distribution is best fit by a three component model comprising a power law component, a normal component, and a gamma component. The power law, with index $p = 3.95 \pm 0.2$, describes the overall trend in the data. The relative increase seen between 1 μm and 18 μm is described by the normal and gamma components. It is tempting, although speculative, to assign the overall linear trend and the increase between 1 μm and 18 μm to the halo and main ring particle distributions respectively. The halo has a relative abundance of sub-micron particles. A power law with a large index value would best describe this distribution. This is in agreement with theory and possible indications from Voyager data (Showalter *et al.* 1987). The main ring, by contrast, has a greater number of larger bodies whose distribution may be more like the combination of the gamma and normal components. The difference in the type of particle size distribution between the ring and halo may suggest that main ring particles are being modified before ejection into the halo. For modification to occur, particles would need to reside in the main ring longer than the previous estimates of 10^2 - 10^3 years. Alternatively, the difference may simply arise from the magnetospheric forces that control the structure of the halo being ineffective for particles larger than a micron. Additional observations are needed at different viewing geometries and phase angles to determine the 3-D dependence of the particle size distribution.

Acknowledgments

The authors would like to acknowledge the kind help and support of Bob Carlson and the NIMS team, especially Frank Leader, Bob Mehlman, Lucas Kamp, and John Hui, without whom these observations would not have been possible. Our thanks also extend to the many engineers and scientists who made the Galileo mission a success. This work was funded by NASA Contract NAS 7-100 to the California Institute of Technology, Jet Propulsion Laboratory.

References

- Becklin, E. E., and C. G. Wynn-Williams 1979. Detection of Jupiter's ring at 2.2 μm . *Nature* **279**, 400-401.
- Burns, J. A., L. E. Schaffer, R. J. Greenberg, and M. R. Showalter 1985. Lorentz resonances and the structure of the Jovian ring. *Nature* **316**, 115-119.
- Burns, J. A., M. R. Showalter, and G. E. Morfill 1984. The ethereal rings of Jupiter and Saturn. In *Planetary Rings* (R. Greenberg and A. Brahic, Eds.), pp. 200-272. Univ. of Arizona Press, Tucson.
- Carlson, R. W. 1981. Spectral Mapping of Jupiter and the Galilean Satellites in the Near Infrared. *SPIE* **268**, Imaging Spectroscopy.
- Carlson, R. W., P. Drossart, Th. Encrenaz, P. R. Weissman, J. Hui, and M. Segura 1997. Temperature, size, and energy of the Shoemaker-Levy 9 G-impact fireball. *Icarus* **128**, 251-274.
- Carlson, R. W., P. R. Weissman, W. D. Smythe, J. C. Mahoney, and the NIMS science and engineering team 1992. The near-infrared mapping spectrometer experiment on Galileo. *Space Sci. Rev.* **60**, 457-502.
- Consolmagno, G. J. 1980. Electromagnetic scattering lifetimes for dust in Jupiter's ring. *Nature* **285**, 557-558.
- Horányi, M. and T. E. Cravens 1996. The structure and dynamics of Jupiter's ring. *Nature* **381**, 293-295.

- Jewitt, D. C., and G. E. Danielson 1981. The Jovian ring. *J. Geophys. Res.* **86**, 8691-8697.
- Jewitt, D. C., G. E. Danielson, and R. J. Terrile 1981. Groundbased observations of the Jovian ring and inner satellites. *Icarus* **48**, 536-539.
- Morfill, G. E., E. Grün, and T. V. Johnson 1980. Dust in Jupiter's magnetosphere: physical processes. *Planet. Space Sci.* **28**, 1087-1100.
- Neugebauer, G., E. E. Becklin, D. Jewitt, R. Terrile, And G. E. Danielson 1981. Spectra of the Jovian ring Amalthea. *Astron. J.* **86**, 607-610.
- Nicholson, P. D., and K. Matthews 1991. Near-infrared observations of the Jovian ring and small satellites. *Icarus* **93**, 331-346.
- Owen, T., G. E. Danielson, A. F. Cook, C. Hansen, V. L. Hall, and T. C. Duxbury 1979. Jupiter's Rings. *Nature* **281**, 442-446.
- Showalter, M. R., J. A. Burns, J. N. Cuzzi, and J. B. Pollack 1985. Discovery of Jupiter's gossamer ring. *Nature* **316**, 526-528.
- Showalter, M. R., J. A. Burns, J. N. Cuzzi, and J. B. Pollack 1987. Jupiter's ring system: New results on structure and particle properties. *Icarus* **69**, 458-498.
- Smith, B. A., *et al.* 1979. The Galilean satellites and Jupiter: Voyager 2 imaging science results. *Science* **206**, 927-950.
- Smythe, W. D., R. Lopes-Gautier, A. Ocampo, J. Hui, M. Segura, L. A. Soderblom, D. L. Matson, H. H. Kieffer, T. B. Mccord, F. P. Fanale, W. M. Calvin, J. Sunshine, E. Barbinis, R. W.

Carlson, and P. R. Weissman 1995. Galilean satellite observation plans for the near-infrared mapping spectrometer experiment on the Galileo spacecraft. *J. Geophys. Res.* **100**, 18957-18972.

Smoluchowski, R., 1976. Origin and structure of Jupiter and its satellites. In *Jupiter* (T. Gehrels, Ed.), pp. 3-21. Univ. of Arizona Press, Tucson.

Wolf, A. A., and D. V. Byrnes 1993. Design of the Galileo satellite tour. Paper presented at the Astrodynamics Specialist Conference, Am. Astron. Soc./Am. Inst. Aeronaut. Astronaut., Victoria, B.C.

Figure Captions

Fig. 1. Calibrated images of the eastern ansa of the Jovian ring system from the Galileo NIMS instrument. Each image covers a portion of the ring from $\approx 1.80R_J$ to just above Jupiter's cloud-tops on the far right. The spatial resolution is 1130 km. Each pixel measures 450km along the ring plane by 1130km out of the ring plane. All data have been converted to dimensionless units of I/F where I is the radiance and F is the solar flux density at Jupiter's distance from the Sun. Figures 1a, 1b, and 1c show the ring system at 1.31, 2.03, and 3.51 μm respectively. The maximum I/F values for these three wavelengths are 8.5×10^{-3} , 11.3×10^{-3} , and 9.8×10^{-3} . Points A, B, C, and D correspond to the locations used in Figures 2 and 3 and are positioned at $1.75R_J$, $1.55R_J$, $1.32R_J$, and $1.09R_J$ respectively.

Fig. 2a-c. Profiles taken through the ring plane at the locations marked A, B, C, and D in Fig. 1. Figures 2a, 2b, and 2c show profiles measured at 1.31, 2.03, and 3.51 μm respectively. For each profile, I/F is plotted for each pixel where a pixel value of zero corresponds to above the ring plane and a pixel value of twenty lies below the ring plane. Each pixel measures 1130km out of the ring plane.

Fig 3. Profiles measured along the ring plane at 1.31, 2.03, and 3.51 μm . Dimensionless I/F is plotted against pixel value measured along the ring plane where a value of zero is furthest from Jupiter. Each pixel measures 450km along the ring plane.

Fig. 4. Spectra measured at locations A, B, C, and D for wavelengths between 1.0 and 4.0 μm . I/F is plotted against wavelength measured in microns.

Fig. 5a-b. Geometry of the Jovian ring system at the time of the NIMS observations.

Figure 5a shows a schematic of the edge-on ring system as viewed by the NIMS instrument. The NIMS data cube was split into two parts depending on whether the halo contributed to the measured signal in that region. Region 1 contains just light scattered by the main ring while region 2 contains light scattered by both the ring and halo. Figure 5b shows a schematic of the Jovian ring system as viewed from above the ring plane. The shaded areas depict the apparent pathlength as seen at two different positions on the ring. The pathlength varies as a function of the projected distance from Jupiter.

Fig. 6. Values of $\omega_0 \tau P(\theta)$ plotted as a function of scattering angle for 10 wavelengths spaced equally between 1.0 μm and 4.0 μm . The solid line represents the observed NIMS data while the dashed line is the calculated values from the scattering model re-normalized by the pathlength.

Fig. 7. Logarithm of the retrieved particle size distribution plotted as a function of logarithm of the particle radius. The number of particles decreases roughly linearly with radius in logarithm space indicative of a power law distribution. A relative increase in the number of particles is also apparent between 1 μm and 18 μm . This feature is best fit by a combined normal and gamma distribution.

Fig. 8. Values of $\tau\omega_0P(\theta)$ plotted as a function of the Voyager scattering angles of 4° to 6° at 12 wavelengths. The two wavelength bands on the left of the figure correspond to the wavelengths of the Voyager violet and orange filters. The remaining 10 near-infrared bands correspond to those NIMS wavelengths chosen during our modeling and in Figure 6. The solid line shows the values calculated using our retrieved particle size distribution and the appropriate phase function for scattering angles between 4° and 6° . The dashed line represents data constructed from a power law distribution with $p = 2.5$. Although the values of $\omega_0\tau P(\theta)$ for the two distributions appear to be nearly the same at optical wavelengths, they diverge towards the infrared.

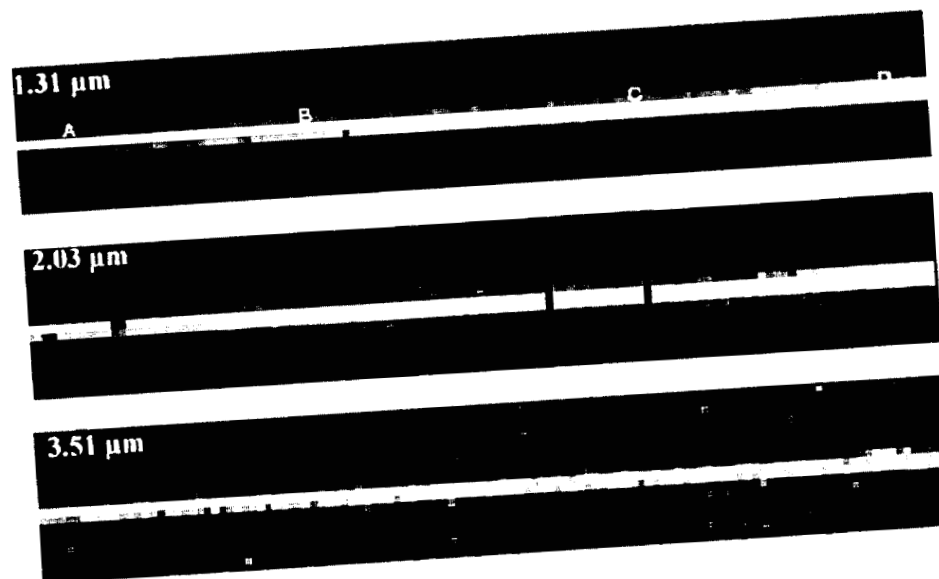


Figure 1: Diffraction patterns at 1.31, 2.03, and 3.51 μm

1.31 μm



2.03 μm



3.51 μm



Figure 1
McMuldloch

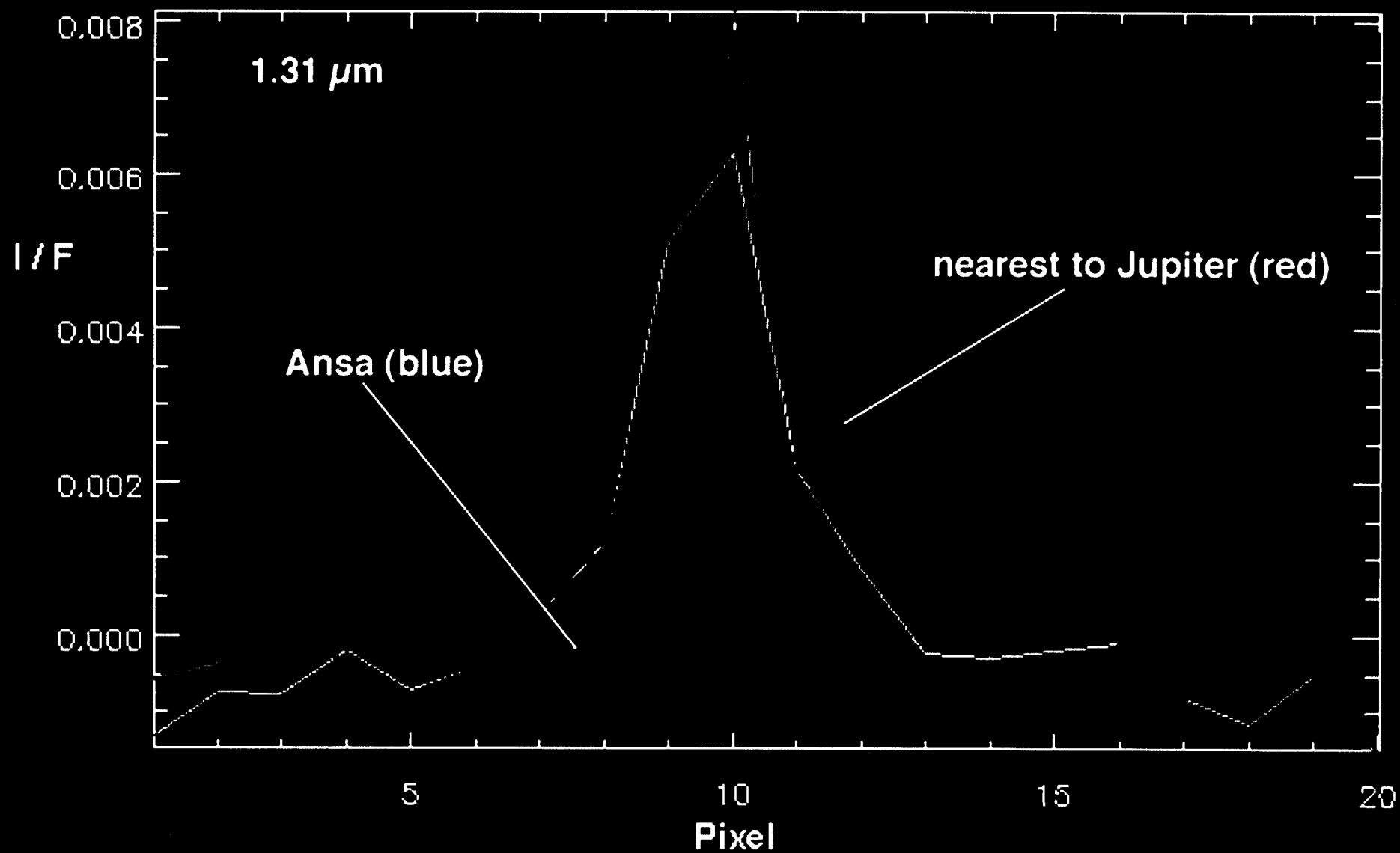


Figure 2a
McMuldloch

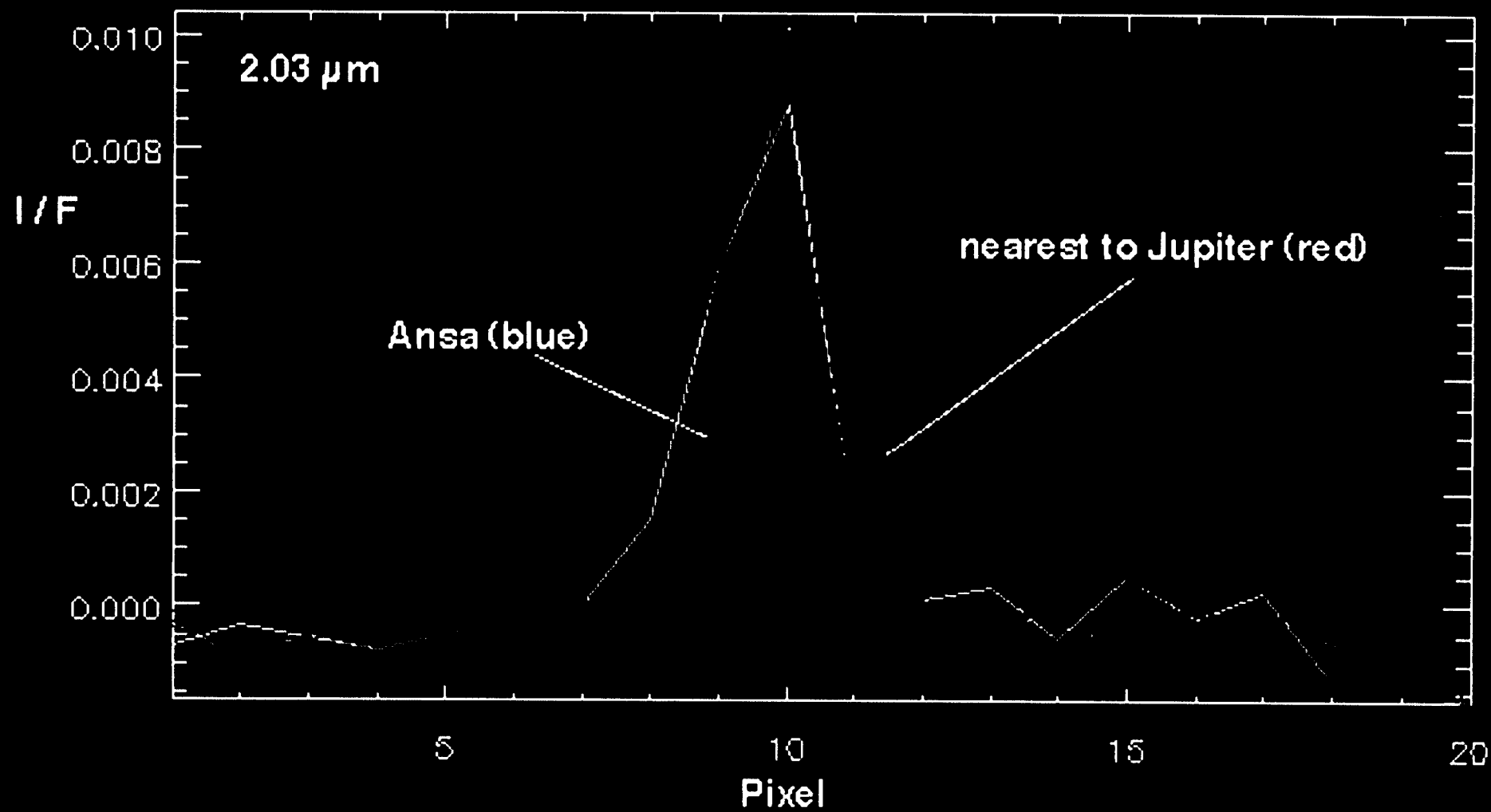


Figure 2b
McMuldach

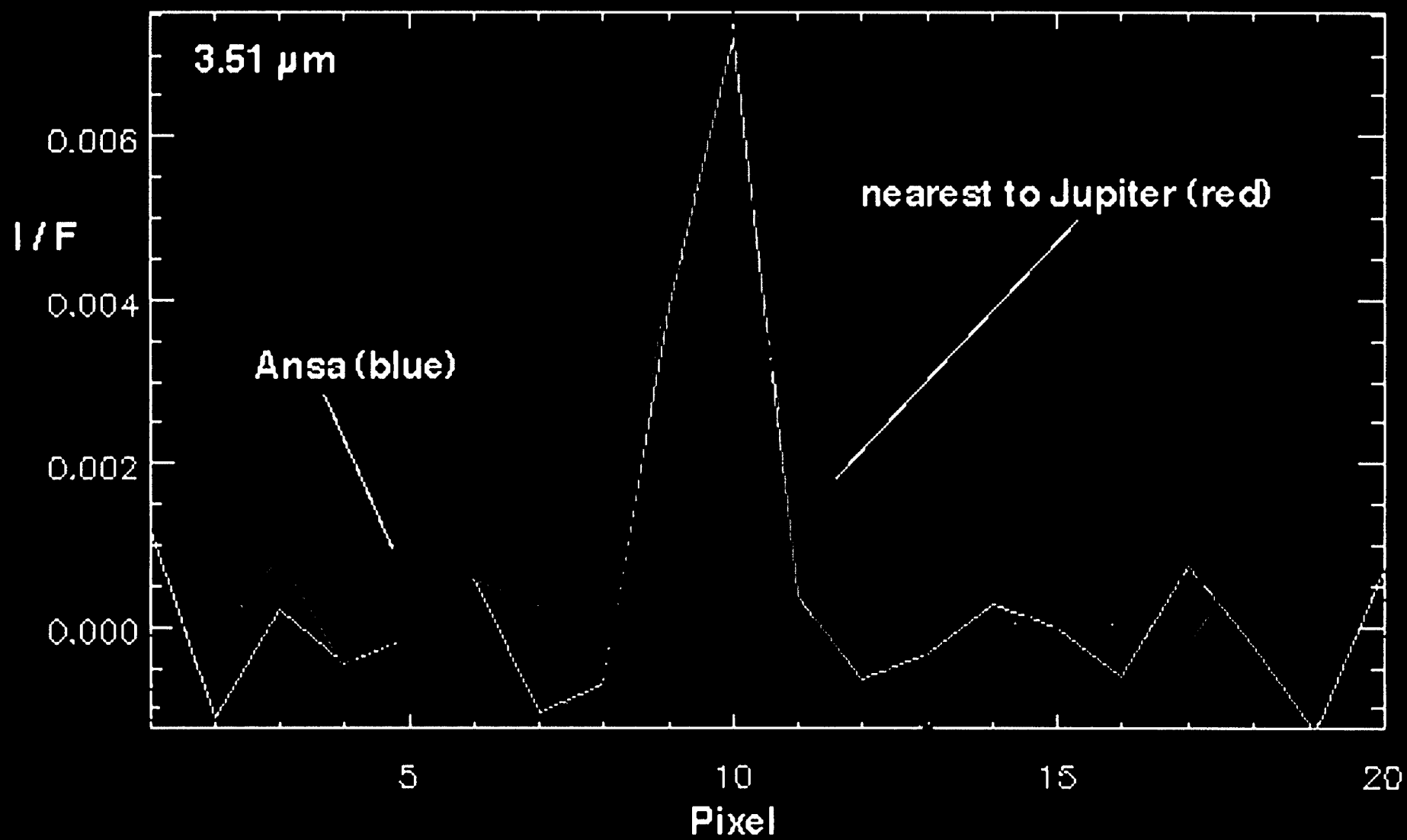


Figure 2c
McMuldorch

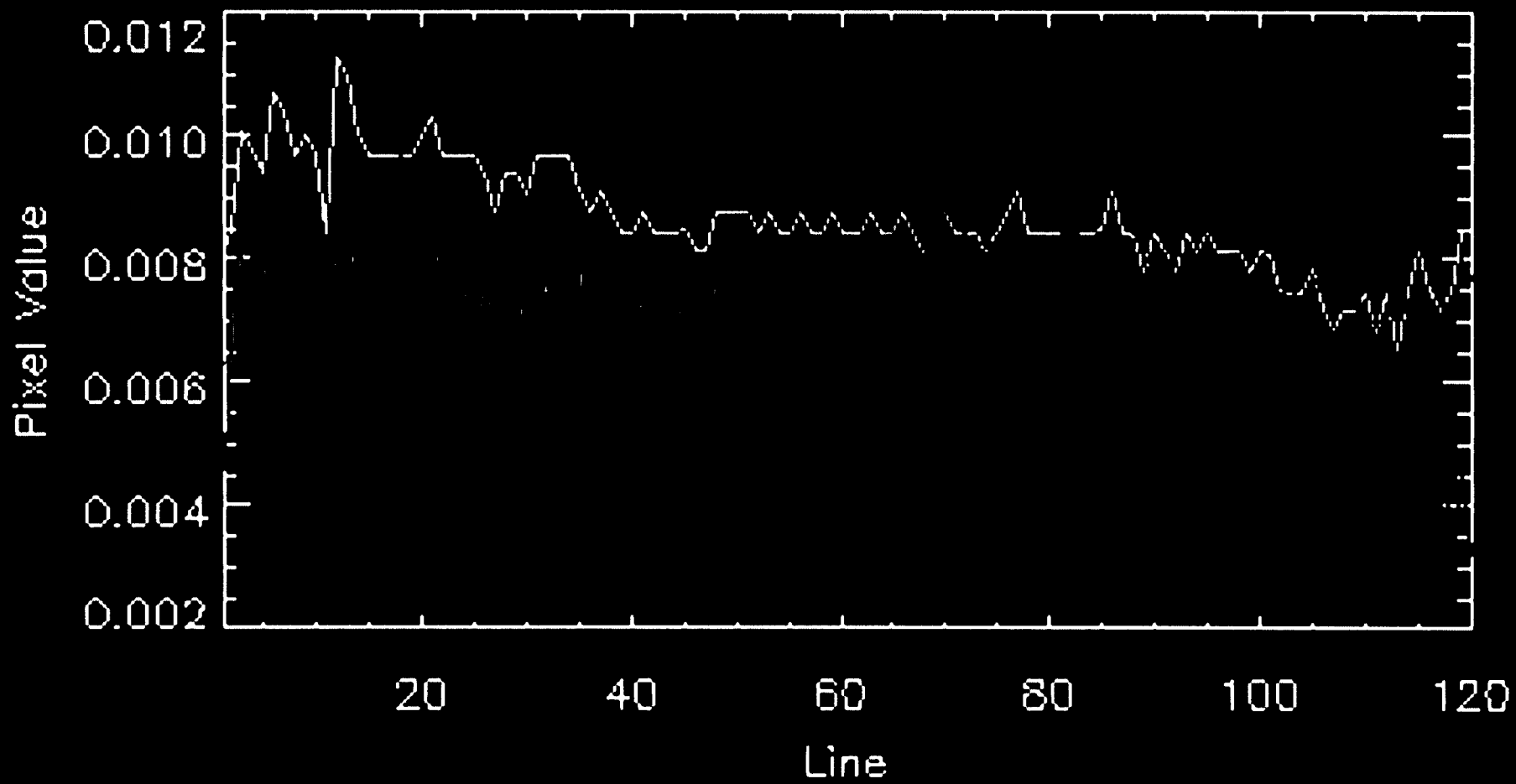


Figure 3
McMuldroch

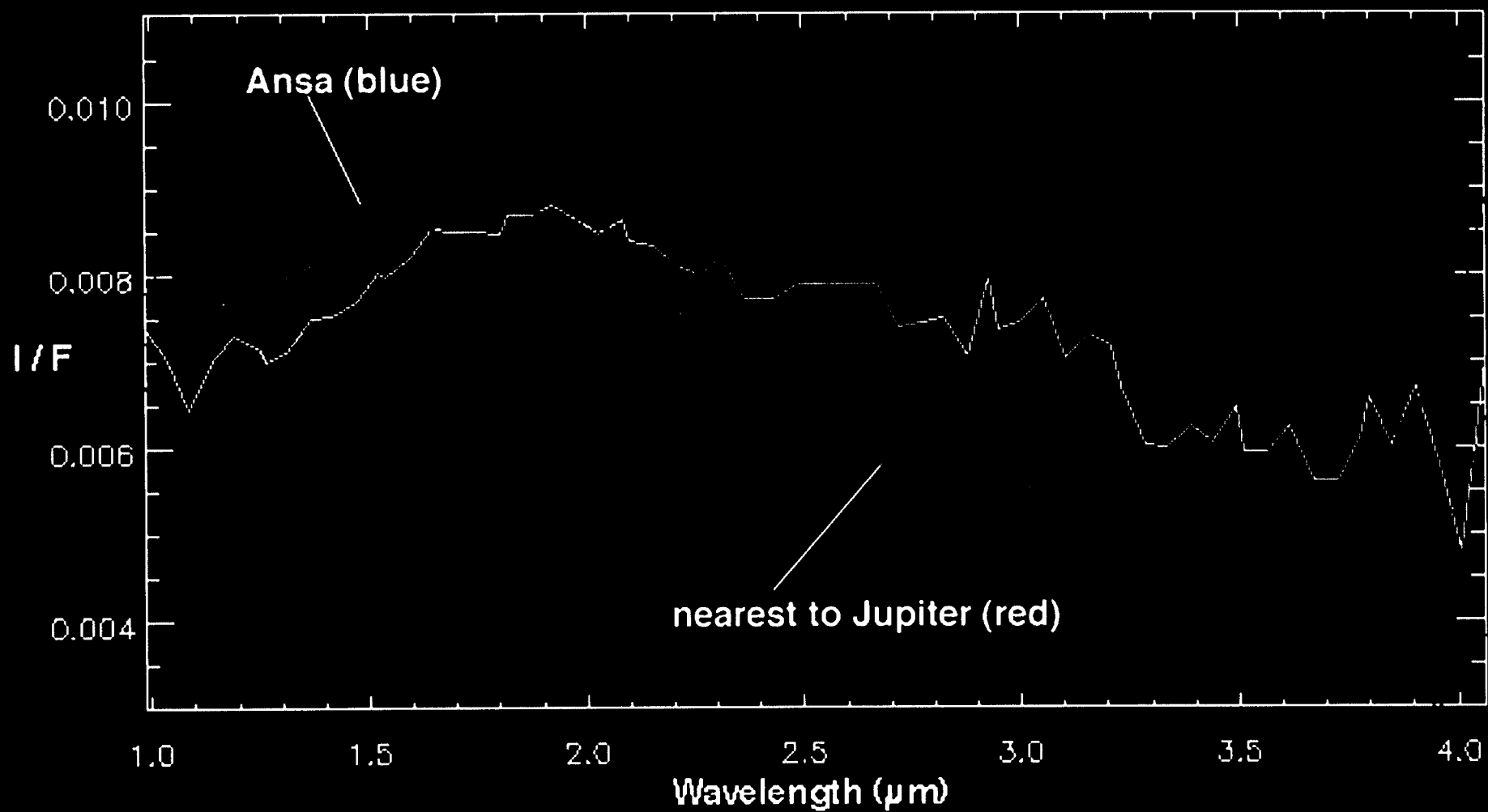


Figure 4
McMuldroch

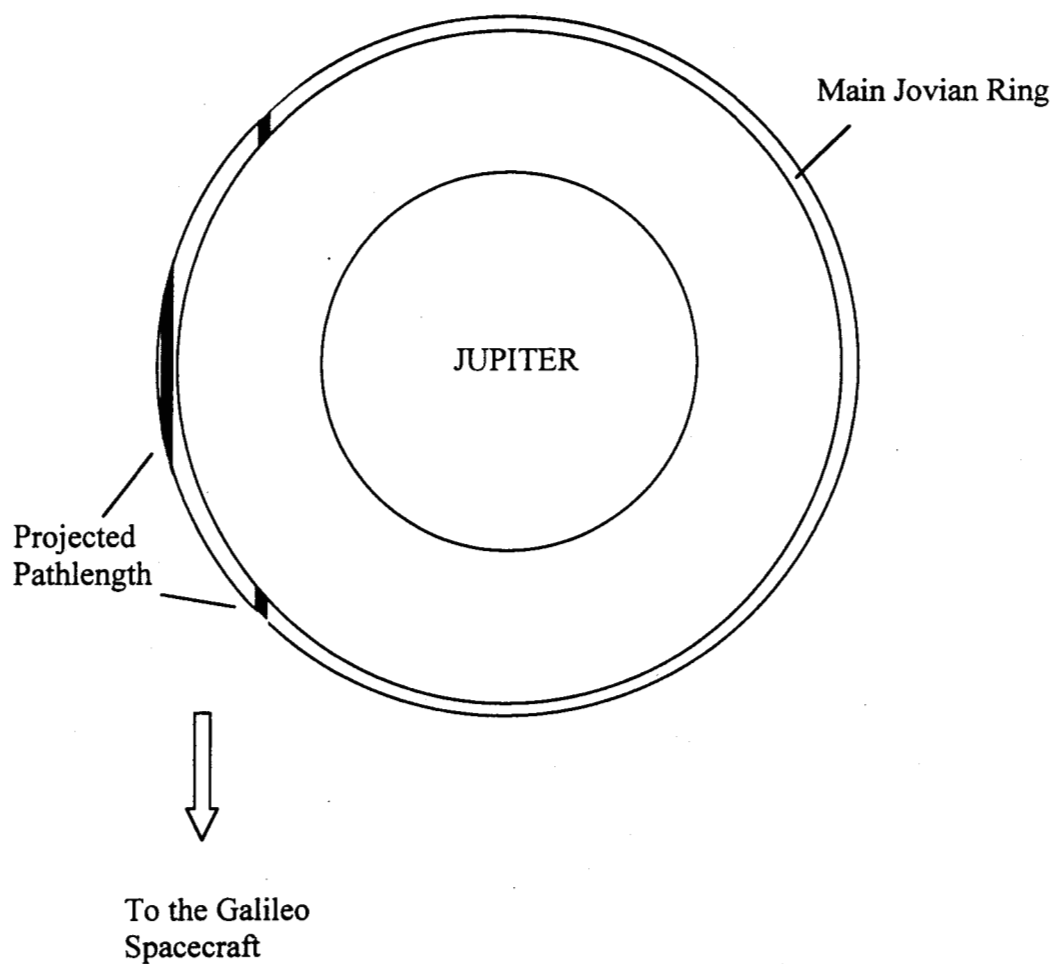
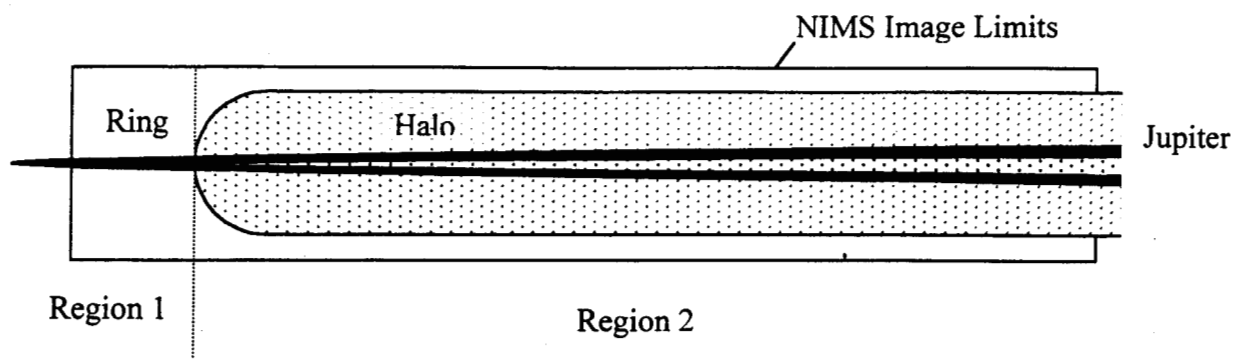


Figure 5
McMuldloch

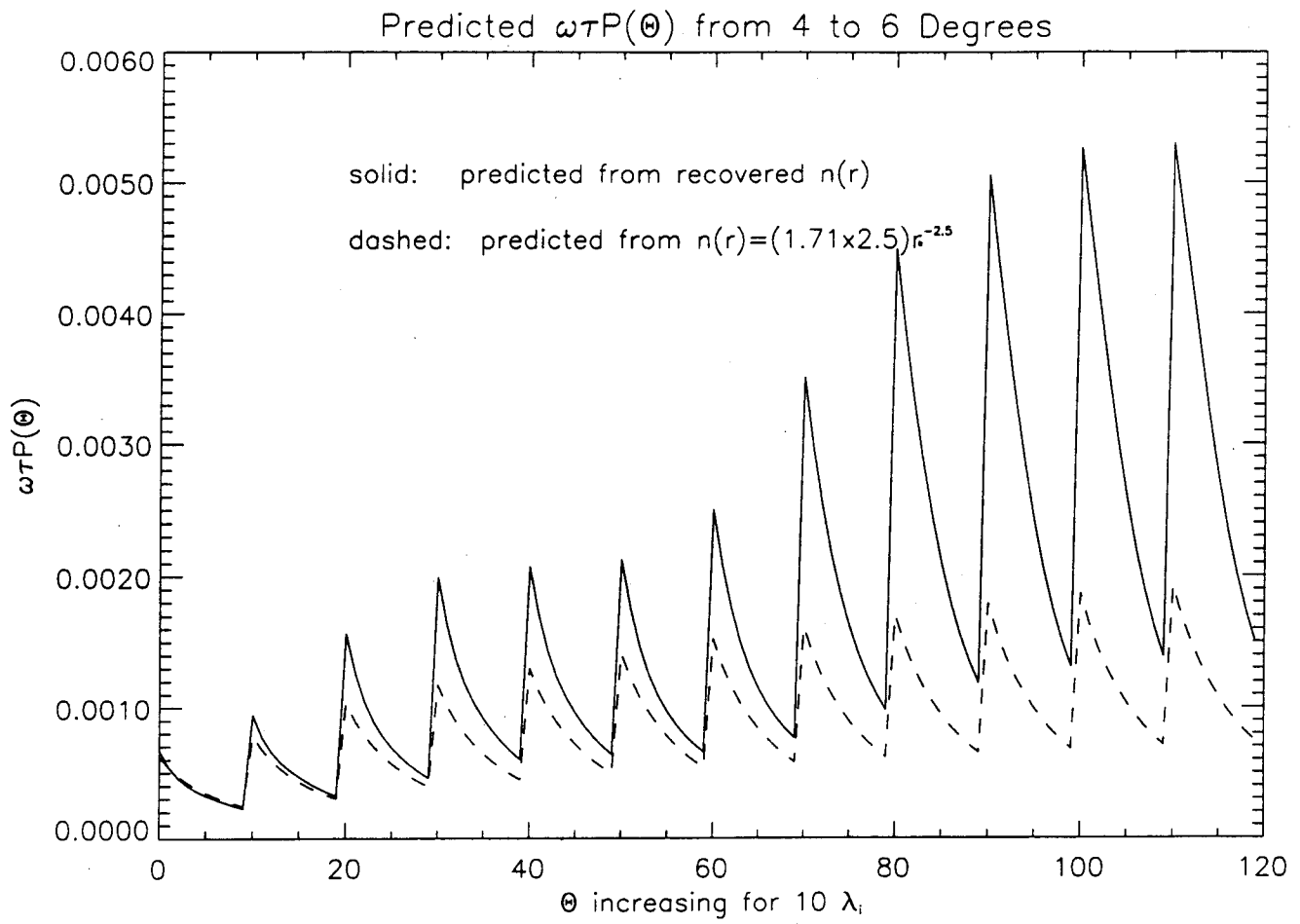


Figure 6
McMuldach

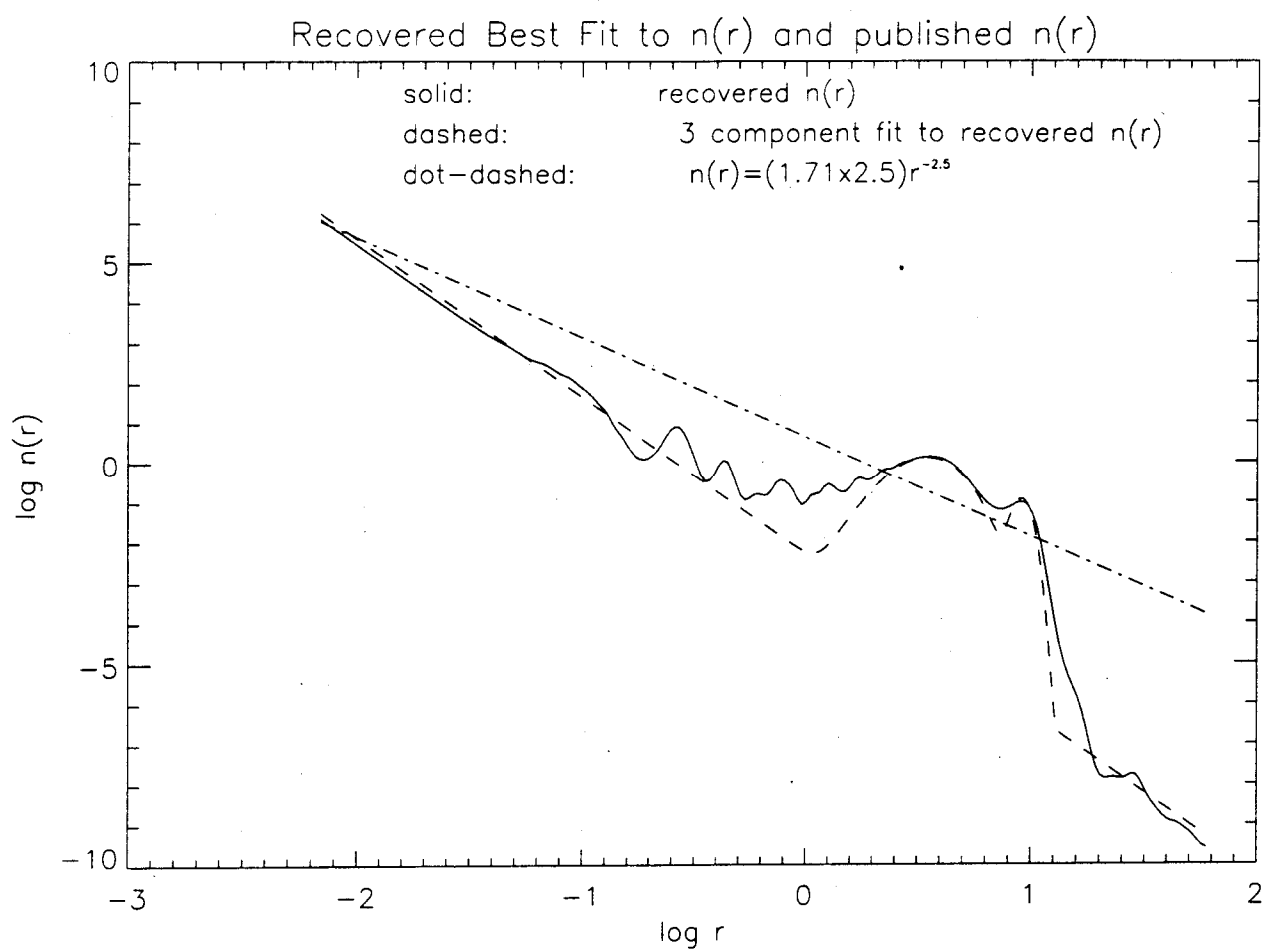


Figure 7
McMuldach

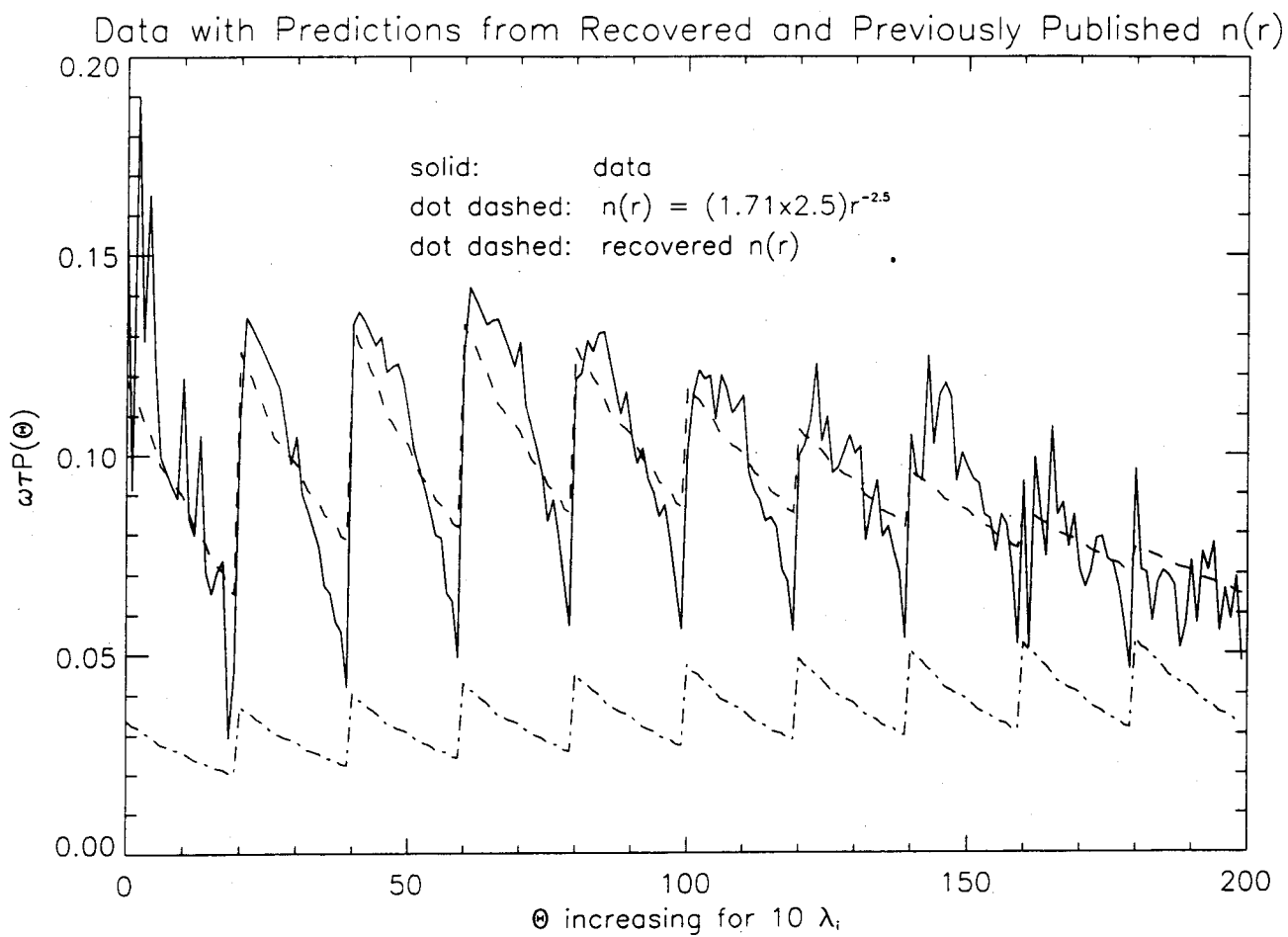


Figure 8
McMuldroch